







MeerKAT view of the dancing ghosts – peculiar galaxy pair PKS 2130–538 in Abell 3785

Velibor Velović ¹★, William D. Cotton ^{2,3}, Miroslav D. Filipović ¹, Ray P. Norris ^{1,4},
Luke A. Barnes ¹ and James J. Condon ²

¹*School of Science, Western Sydney University, Locked Bag 1797, Penrith South DC, NSW 2751, Australia*

²*National Radio Astronomy Observatory, 520 Edgemont Road, Charlottesville, VA 22903, USA*

³*South African Radio Astronomy Observatory (SARAO), 2 Fir Street, Black River Park, Observatory, Cape Town 7925, South Africa*

⁴*CSIRO Space and Astronomy, Australia Telescope National Facility, PO Box 76, Epping, NSW 1710, Australia*

Accepted 2023 April 28. Received 2023 April 27; in original form 2022 November 15

ABSTRACT

We present MeerKAT *L*-band (886–1682 MHz) observations of the extended radio structure of the peculiar galaxy pair PKS 2130–538 known as the ‘Dancing Ghosts’. The complex of bending and possibly interacting jets and lobes originate from two active galactic nuclei hosts in the Abell 3785 galaxy cluster, one of which is the brightest cluster galaxy. The radio properties of the PKS 2130–538 – flux density, spectral index, and polarization – are typical for large, bent-tail galaxies. We also investigate a number of thin extended low surface brightness filaments originating from the lobes. South-east from the Dancing Ghosts, we detect a region of low surface brightness emission that has no clear origin. While it could originate from the Abell 3785 radio halo, we investigate the possibility that it is associated with the two PKS 2130–538 hosts. We find no evidence of interaction between the two PKS 2130–538 hosts.

Key words: galaxies: active – galaxies: clusters: general – galaxies: jets – radio continuum: galaxies – radio continuum: general.

1 INTRODUCTION

The new generation of radio telescopes, including MeerKAT and Australian Square Kilometre Array Pathfinder (ASKAP), is discovering new objects and imaging them in greater detail than ever before (Norris et al. 2021, 2022; Filipović et al. 2022; Heywood et al. 2022). Their wide-area coverage, in combination with the high sensitivity and spatial sampling, enables us to detect low surface brightness features and objects.

One such complex object is the peculiar galaxy pair PKS 2130–538 (named as the Dancing Ghosts by Norris et al. 2021, see their fig. 21). This extended radio source has been previously detected in high-resolution radio continuum surveys (Ekers 1970; Schilizzi & McAdam 1975; Jones & McAdam 1992) and reported as two radio galaxies (G4Jy 1704, 1705) by White et al. (2020a, b).

Based on the ASKAP Pilot Survey, Norris et al. (2021) argued that PKS 2130–538 consists of two galaxies in the galaxy cluster Abell 3785, with possibly interacting radio lobes. The northern ‘Host 1’, also identified as WISEA J213406.70-533418.7, sits in the centre of the northern radio bridge between two lobes at a photometric redshift of $z = 0.078$ (with a comoving distance of $D_c \approx 328$ Mpc). ‘Host 2’, identified as WISEA J213417.69–533811.1, is located in the south-east at a photometric redshift of $z = 0.076$ ($D_c \approx 320$ Mpc) (Bilicki et al. 2014). We adopt a flat Λ CDM cosmological model with $H_0 = 70 \text{ km s}^{-1} \text{ Mpc}^{-1}$, $\Omega_m = 0.3$, and $\Omega_\Lambda = 0.7$. At the redshift of Abell 3785 ($z = 0.0773$), we have $1 \text{ arcsec} = 1.464 \text{ kpc}$.

Norris et al. (2021, see their fig. 21) indicated that the radio spectral index properties of PKS 2130–538 are consistent with a bent-tail galaxy. At the position of Host 1, there is a flat-spectrum region ($\alpha \approx 0$)¹ that connects to the relatively flat-spectrum jets ($\alpha \approx -0.4/ -0.5$). These connect to large bright regions with spectral index $\alpha \approx -0.6$ to -0.7 , which steepens sharply as the lobes and tails change direction to the south to at least ($\alpha \approx -1.5$). Examination of the southern host shows a sudden change in the spectral index. Similar to the northern Host 1, it has a flat spectral index core and steeper spectral index lobe and tail structures.

Norris et al. (2021) were uncertain as to whether there is any interaction between the two hosts and their jets. They also noted a thin stream of emission extends from the north-eastern lobe with a median spectral index of $\alpha \approx -2.1$, which is not expected in existing radio galaxy models.

This paper is organized as follows: in Section 2, we present data used in this study, while in Section 3 we analyse MeerKAT observations of Abell 3785, followed by a detailed analysis of PKS 2130–538 galaxy pair in Sections 3.1. In Section 4, we discuss the results and possible interaction between the two hosts. Finally, we present our conclusions in Section 5. Throughout the paper, we strictly use coordinates of the equinox and epoch J2000.

¹Radio spectral index α is defined as $S_\nu \propto \nu^\alpha$, where S_ν is the flux density at frequency ν .

* E-mail: v.velovic@westernsydney.edu.au

Table 1. Channelization and frequency details of 5 per cent fractional bandwidth subbands used to produce the final images.

Channel	Low (MHz)	Centre (MHz)	High (MHz)
1	886.3	908.0	929.8
2	930.6	952.3	974.0
3	974.9	996.6	1018.4
4	1019.2	1043.5	1067.7
5	1068.5	1092.8	1117.0
6	1117.9	1144.6	1171.4
7	1172.2	1198.9	1225.7
8	1226.5	1255.8	1285.0
9	1285.9	1317.2	1348.6
10	1349.4	1381.2	1412.9
11	1413.8	1448.0	1482.3
12	1483.2	1519.9	1556.7
13	1557.6	1593.9	1630.3
14	1631.1	1656.2	1681.3

2 DATA

South Africa’s MeerKAT radio telescope is a precursor to the Square Kilometre Array (SKA). It consists of 64 antennas, each 13.5 m in diameter (Jonas & MeerKAT Team 2016). Observations of PKS 2130–538 were conducted on 2021 November 28 in *L* band ($\nu = 1283$ MHz; bandwidth of 800 MHz) in 4k mode, for 10 h including calibration. We used 61 of the 64 antennas.

For calibration, we used the pipeline of Mauch et al. (2020), followed by polarization calibration. We used J1939–6342 as a delay, bandpass, and leakage calibrator, while J2214–3835 was used for complex gain and a leakage calibrator. Finally, we calibrated the residual X–Y phase difference using 3C138 and 3C286. The final spectrum, the total intensity at the reference frequency and spectral index, in pixels with adequate signal-to-noise ratio (SNR), was determined by a weighted least-squares fit of the pixel values in the subband images. Pixels without adequate SNR used the weighted average in frequency.

Final images were produced and cleaned using the OBIT/MFIMAGE (Cotton et al. 2018) using the robust weighting of -1.5 , with 5 per cent fractional bandwidth subbands for Stokes I and 1 per cent fractional bandwidths for Stokes Q and U with joint Q/U deconvolution. 1 and 5 per cent fractional bandpass means that each subband had a bandwidth of 1 and 5 per cent of the central frequency. All 14 channels with 5 per cent fractional bandwidth subbands are given in Table 1. We applied frequency-dependent tapering to equalize the spatial resolution across the bandpass. The resulting image (Fig. 1) has a synthesized beam size of 7.5×7.1 arcsec² at PA = 0.82° and the local root mean squared (rms) noise $1\sigma = 5.5 \mu\text{Jy beam}^{-1}$.

The wide bandwidth of the MeerKAT *L*-band data allows a Faraday synthesis analysis following that described in Rudnick & Cotton (2023). This analysis uses a reference wavelength $\lambda_0 = 0$ that results in the complex Faraday point spread function (PSF) given in the upper panel of Fig. 2. The high sidelobes from the spectral regions being blanked due to radio frequency interference (RFI) require a complex deconvolution (CLEAN) to recover the Faraday spectrum. The full width at half-maximum (FWHM) of the restoring function is 16 rad m^{-2} (rms = 6 rad m^{-2}). The Faraday analysis used 2 rad m^{-2} elements covering the range $\pm 500 \text{ rad m}^{-2}$ and corrected for an assumed spectral index of $\alpha = -0.7$. The Faraday synthesis (Brentjens & de Bruyn 2005) was performed using OBIT task RMSYN. Following Rudnick & Cotton (2023), we use a restoring function for the width of the inner real lobe of the ‘dirty’ PSF as shown in the lower panel of Fig. 2.

In addition to MeerKAT data, we also used ASKAP data from Evolutionary Map of the Universe (EMU) survey described in Norris et al. (2021) and optical data from the DESI Legacy Imaging Surveys (Dey et al. 2019).

3 RESULTS

Figs 1, 3, 4, and 5 show total intensity images of PKS 2130–538 as observed by MeerKAT at a nominal frequency of $\nu = 1283$ MHz. PKS 2130–538 is a member of the galaxy cluster Abell 3785, which consists of 47 members and is classified as a compact cluster (type II) by the Bautz–Morgan system, with richness class 0 (Bautz & Morgan 1970; Abell, Corwin & Olowin 1989). Host 2 is the brightest cluster galaxy (BCG) of this cluster (Lauer et al. 2014). Abell 3785 centre, marked with ‘X’ in Fig. 3, is positioned at RA = 21:34:30, Dec. = $-53:37:0$ at the redshift of $z = 0.0773$ ($D_c \approx 325$ Mpc) and velocity dispersion of $\sigma_v = 897 \pm 312 \text{ km s}^{-1}$ (Lauer et al. 2014). There are no previous observations or information on Abell 3785 in X-ray catalogues.

We consider sources to belong to the Abell 3785 cluster if their position is within a cluster radius, defined by Abell et al. (1989) as $R_A = (1.7/z_A) = 22$ arcmin (dashed circle in Fig. 3), and their redshift is between $z = 0.055$ and $z = 0.095$. We detect 30 sources whose redshifts (Jones et al. 2009; Bilicki et al. 2014) and spatial position fit these criteria. These 30 members of the Abell 3785 cluster, including the Dancing Ghosts, are marked as red circles in Fig. 3. We also note a deficit of cluster members west of the Dancing Ghosts.

The Dancing Ghosts complex spreads over ≈ 7.1 arcmin, corresponding to ≈ 624 kpc at the distance of Abell 3785. There is a region of diffuse emission to the bottom left (south-east) of the PKS 2130–538 (marked with the blue polygon in Fig. 3, bottom right inset). This region is discussed in Section 4.2. In that subsection, we also discuss radio object WISEA J213541.80–534413.2 as a potential cause of the diffuse emission, which is positioned 12 arcmin east from the Dancing Ghosts (Fig. 3 top left). Finally, two other interesting Abell 3785 members with extended emission (Fig. 3 top right) are positioned 17 arcmin north of the Dancing Ghosts and discussed in more detail in Section 4.4.

3.1 Morphology

Norris et al. (2021) established that radio emission from PKS 2130–538 is most likely coming from two active galactic nuclei (AGNs), northern (Host 1) and southern (Host 2), marked in Fig. 4 as H1C and H2C.

Both the northern and southern sources have symmetric and narrow inner jets (marked in Fig. 4 as H1J and H2J). After the initial linear flow, jets of the northern host (Host 1) form large lobes (H1L-E and H1L-W). We see this effect in a number of other AGNs (Hardcastle & Croston 2020).

Lobes associated with the northern source extend southwards, forming a low surface brightness structure and wide tails that are marked in Fig. 4 as H1WT-E and H1WT-W. We also note that both lobes and right wide tail (H1L-E, H1L-W, H1WT-W) show multiple low surface brightness filaments (or wisps; see Fig. 4 marked as H1Wisp1 to H1Wisp4) extending in the north-east direction.

Relatively close (15 arcsec) to the core of the Host 2 (H2C), we see the eastern jet of Host 2 forming a lobe (H2L-E), which bends as it propagates towards Host 1 (H2WT-E). The Host 2 western jet propagates a relatively short distance before forming a circular lobe (H2L-W). The distance to the lobe appears shorter than in the eastern jet. There is some indication of the jet propagation after

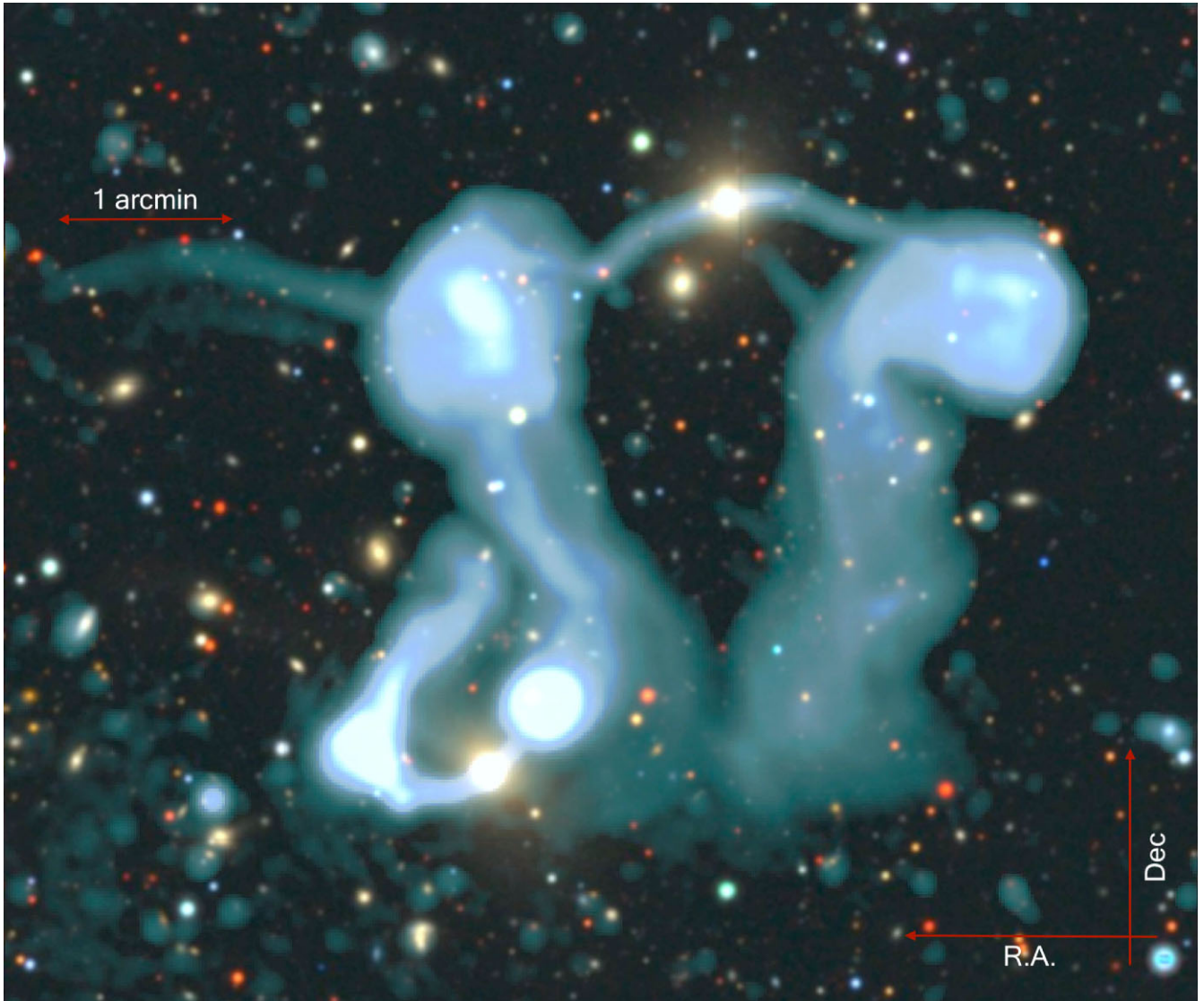


Figure 1. The total intensity image of PKS 2130–538, observed by MeerKAT at $\nu = 1283$ MHz, split into three contrast levels and superimposed over the optical image obtained from the Dark Energy Survey (DES) legacy survey. To present the radio filamentary structure of the Dancing Ghosts, we adjusted linear contrast levels and applied a logarithmic colour scale. We also applied different linear colour maps to enhance the filamentary and diffuse structure of the Dancing Ghosts. For all quantitative information refer to Figs 3–6.

the lobe, but it is surrounded by the wide tail from the Host 1 (H1WT-E).

In Fig. 6, we compare MeerKAT (left-hand column) with ASKAP (right-hand column) images of PKS 2130–538. We zoom into three specific regions, marked in Fig. 4 as A, B, and C. Notably, MeerKAT observations have increased sensitivity and resolution compared to the ASKAP observations. There is an excellent agreement between MeerKAT and ASKAP images, although MeerKAT also detects subtle variations in low surface brightness structures. Orange contours are from the MeerKAT total intensity image, while cyan contours represent total intensity from ASKAP image.

In region A (top panel and Fig. 4), MeerKAT detects a hotspot (Fig. 6 top left panel) before the jet reaches the upper left lobe. This is similar to the Hydra A (3C 218) in the Hydra galaxy cluster (Abell 1060, Taylor et al. 1990). In region B (middle panel), we see an elongated wisp (H1Wisp1 in Fig. 4) in both images. In addition, slightly below this wisp, MeerKAT is able to distinguish another low

surface brightness feature (wisp, H1Wisp2) with a similar direction and shape. In the third region (C; bottom panel), we see more details and structure of the wide tails (H1WT-E and H1WT-W in Fig. 4) in the MeerKAT image. H1WT-E is a region where there may be an interaction between the jets originating from different hosts.

3.2 Spectral index

Fig. 7 shows the spectral index image of PKS 2130–538 calculated using MeerKAT images in 14 sequential channels from 886 to 1681 MHz. The details of channelization are given in Table 1. The spectral index value is presented if the reduced chi-squared statistic ($\chi^2_\nu = \chi^2/\nu$) when fitting the spectral index is no worse than the straight average assuming the default spectral index (0).

We measured flux densities using the method described in Filipović et al. (2022). We carefully selected regions that exclude all

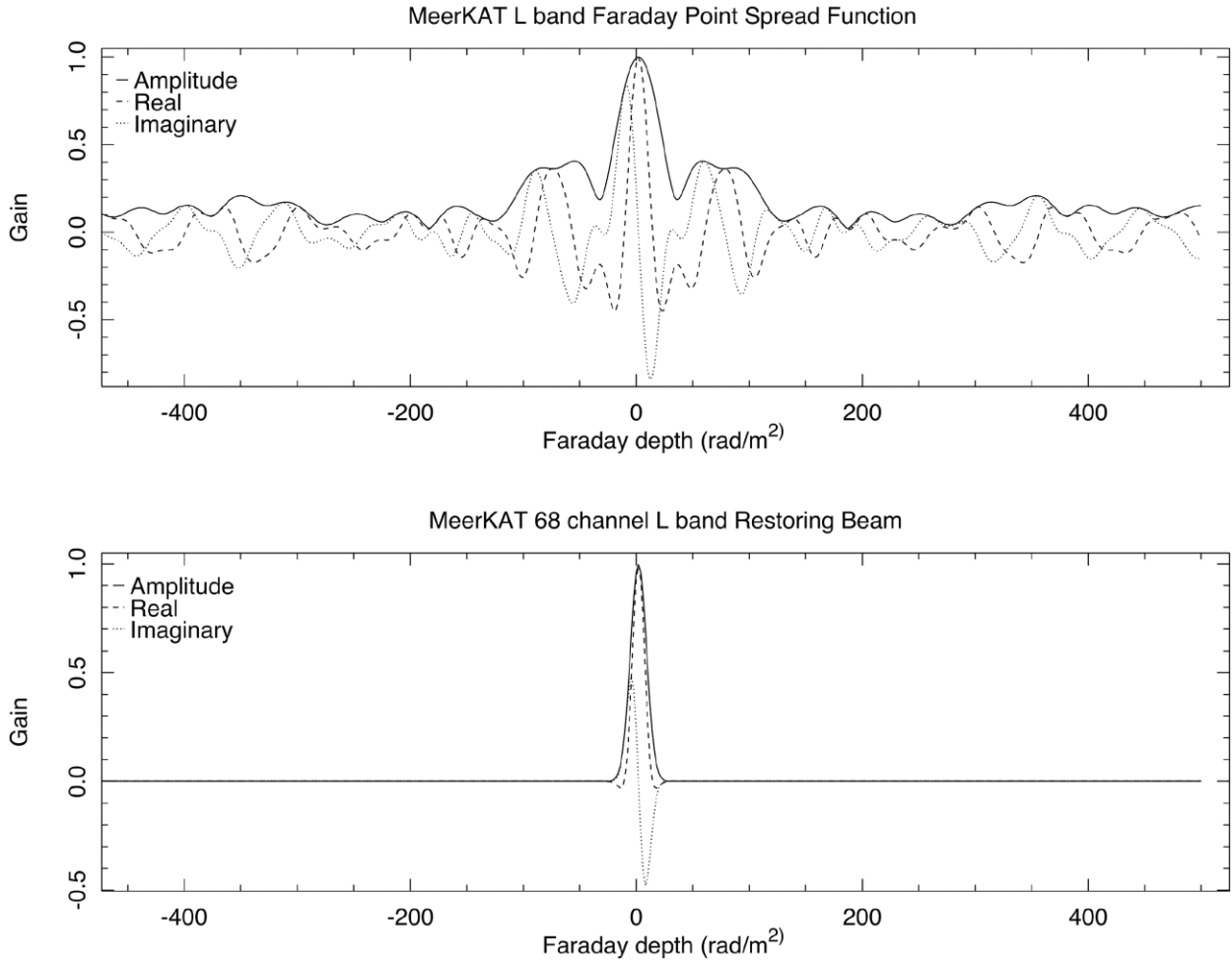


Figure 2. Top panel: The complex ‘dirty’ Faraday PSF for MeerKAT *L*-band data. The amplitude, real, and imaginary parts are shown as solid, dashed, and dotted lines. Bottom panel: The restoring function used for the deconvolved Faraday spectra. The width of the amplitude is that of the real component in the upper panel.

obvious point sources and measured the total radio flux density, accounting for the local background of a region with POLYGON selection package from the Cube Analysis and Rendering Tool for Astronomy (CARTA; Comrie et al. 2021). We note the selected regions have low surface brightness and/or are sometimes embedded in other complex environments. This may significantly influence the accuracy of our measurements. Similarly, we used the same method and regions to estimate the average spectral index using the image shown in Fig. 7. We estimate that our flux density measurements have an overall scale error of ≈ 10 per cent. Our measurements are shown in Table 2.

The spectral index in the cores of the two Hosts (1 and 2) are $\alpha_{\text{HIC}} = +0.2$ and $\alpha_{\text{H2C}} = -0.3$. AGN cores often have a flat or inverted spectral index as a result of free-free absorption and synchrotron self-absorption originating in the presence of optically thick plasma (Donnelly, Partridge & Windhorst 1987; Prandoni et al. 2006).

Jets propagating from both hosts display a spectral index of $\alpha = -0.7$, extending all the way to the central region of four lobes. In the lobes, the mean spectral index in the central part is $\alpha \approx -0.8$ and steepens towards the edges to $\alpha = -1.1$. Spectral indices in the tails and wisps are even steeper, ranging from -1.5 to under $\alpha \leq -2.2$. Except in the AGN cores, the spectral index values calculated

using MeerKAT data are slightly steeper than the spectral index from the previous study of the Dancing Ghosts (Norris et al. 2021) (see Section 1). However, it is still consistent with bent-tail galaxies in general.

The New MeerKAT image reveals more of the low surface brightness with enough SNR to calculate the spectra in the tails below -1.5 , which was noted as a limit in the ASKAP observation by Norris et al. (2021). In the regions of jets and lobes, we see a consistency of spectral index between the two observations, within the range of uncertainties. A potential reason for a steeper spectral index in the new image might be the wider bandwidth of the MeerKAT telescope, which is 860 MHz, compared to the ASKAP observation with a bandwidth of 288 MHz.

From the four detected wisps shown in Fig. 4, we estimate the spectral index from wisp 1 and wisp 2 to be $\alpha \leq -2.2$. This is similar to what Ramatsoku et al. (2020) found in ESO 137–006 as $\alpha \approx -2$.

3.3 Polarization and Faraday rotation analysis

We produced the fractional polarization (FPol) using a peak Faraday de-rotated polarized intensity (PPol) map and Stokes I image at nominal frequency $\nu = 1283$ MHz. Each pixel in the polarized intensity cube was required to have at least a 5σ value in

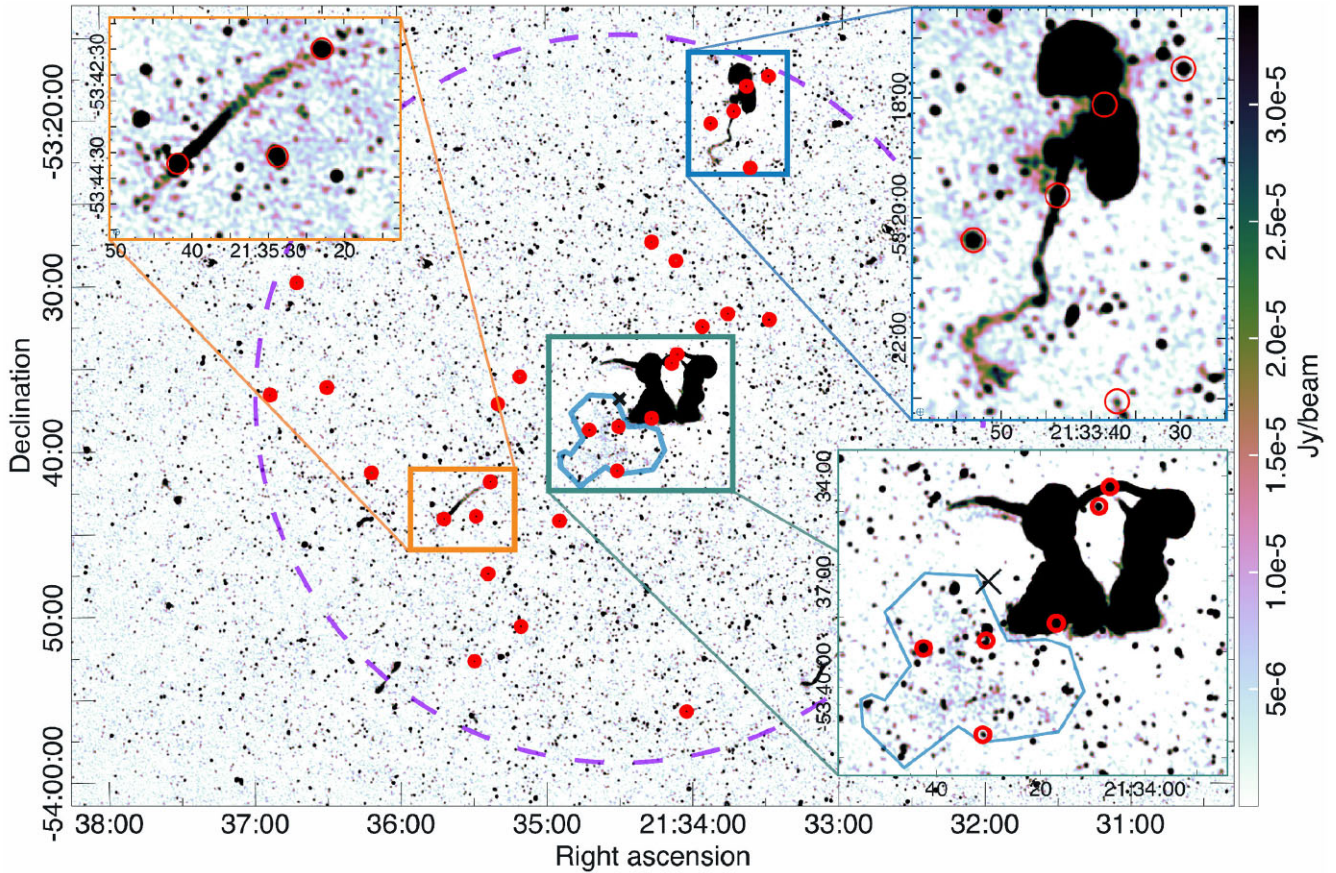


Figure 3. MeerKAT image of the Dancing Ghosts field and the galaxy cluster Abell 3785. The dashed purple circle with a 22 arcmin radius marks the border of Abell 3785, with the centre of the cluster marked with a black ‘X’ in the green square. 30 radio continuum members of the Abell 3785 galaxy cluster are marked with red circles. The inset images are at the same intensity scale (colour bar) as the main image. The blue polygon marks the low surface brightness emission and three radio point sources belonging to the Abell 3785 galaxy cluster, just south of PKS 2130–538. The synthesized beam size (FWHM of the PSF) is 7.5×7.1 arcsec² at PA = 0.82° and the rms is $\sigma = 5.5 \mu\text{Jy beam}^{-1}$.

one or more planes else the pixel was blanked. We then calculated the fractional polarization as a ratio between the two maps $FPol = PPol/I$.

The leftmost panel in Fig. 8 shows the fractional polarization map of the Dancing Ghosts overlaid with total intensity contours. The fractional polarization of all jets in the Dancing Ghosts structure is below 10 percent. We note that regions of H1WT-E, H2L-W and the lower part of H1L-E have low fraction polarization, about 4–5 percent. Other lobes and wide tails have varying fractional polarization up to 20 percent, which is common in AGN with bent-tail jets (Ishwara-Chandra et al. 1998). The low integrated fractional polarization appears to be the result of a complex mixture of emitting regions and Faraday screens.

Interestingly, we detect the highest fractional polarization within a wisp H1Wisp1 on the north-east side and H1Wisp3 reaching up to 50 percent polarized emission. We will further discuss the polarization and spectral index properties of the H1Wisp1 in Section 4.3.

The peak rotation measure (RM) cube is given in the middle panel of Fig. 8. This figure shows a patchy structure covering a wide range of Faraday depths and the locations of the sightlines used to obtain Faraday amplitude spectra.

Fig. 9 shows the Faraday amplitude spectra at a number of sightlines. These sightlines through the inner sources are indicated by the black symbols in the middle panel of Fig. 8. Spectra on a

nearby AGN (Fig. 9a) and a polarized knot in the inner jet of the northern source (Fig. 9b) show simple, single, unresolved Faraday components. Sightlines through the lobes (Figs 9c–9f) show multiple components spread over up to 100 or more rad m^{-2} . These Faraday thick structures will certainly contribute to the depolarization seen in the extended regions of the central sources in Fig. 8.

3.3.1 Faraday width

Many of the sightlines whose Faraday spectra are shown in Fig. 9 show an extended response in Faraday depth. The rms width of the Faraday response in pixels with significant polarized emission is given in Fig. 8. Note, the rms width of the restoring function used in the CLEAN is about 6 rad m^{-2} . Requirements for pixels in the rightmost panel in Fig. 8 to have a non-blank value must meet certain criteria. The pixel must have at least one plane with a value greater than $25 \times$ rms value of the plane, and it must have more than 20 percent of the peak value in the spectrum in that pixel. Additionally, the maximum value in the spectrum for each pixel must be above $30 \mu\text{Jy}$ and the integral values over non-blanked pixels must exceed $100 \mu\text{Jy}$. The presented width in Faraday depth will substantially depolarize the emission.

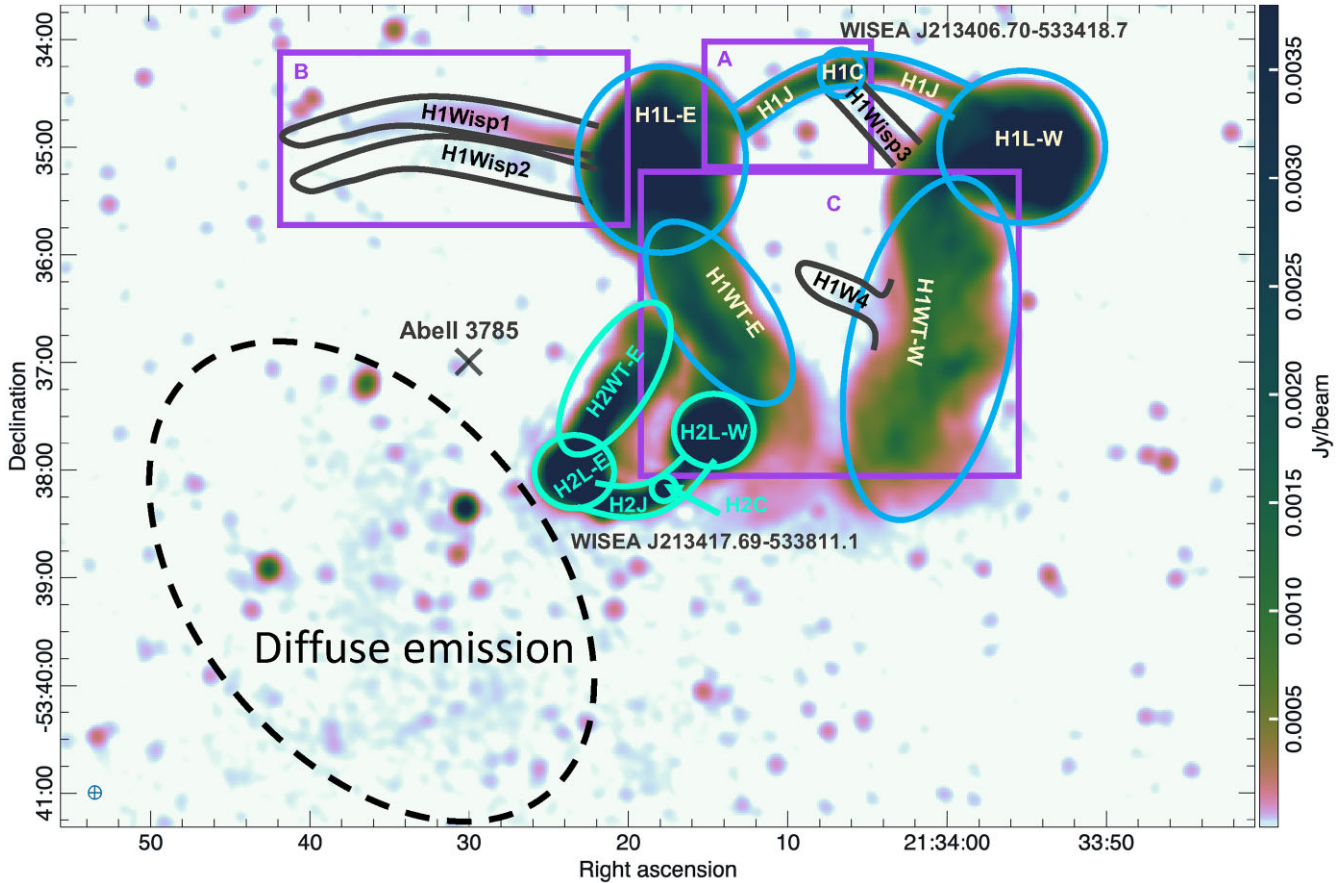


Figure 4. Total intensity image of PKS 2130–538 obtained with MeerKAT at nominal frequency of $\nu = 1283$ MHz. We used a logarithmic function to enhance low surface brightness. Legend: Host 1 (H1): H1C – core, H1J – jets, H1L(W, E) – lobes, H1Wisp(1,2,3,4) – wisps, H1WT(W, E) – wide tails; Host 2 (H2): H2C – core; 8) H2L(W, E)-lobes 9) H2WT-E wide tail 10) dashed ellipse show the diffuse emission related to the source. The ‘X’ marks the centre of Abell 3785. In the bottom left corner, we show the synthesized beam size of 7.5×7.1 arcsec² at PA = 0.82° .

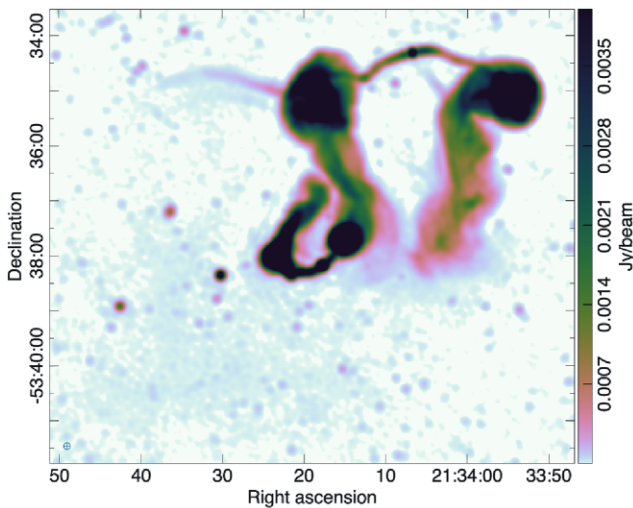


Figure 5. Total intensity image of the Dancing Ghosts obtained with MeerKAT at a nominal frequency of $\nu = 1283$ MHz. In the bottom left corner, we show the synthesized beam size of 7.5×7.1 arcsec² at PA = 0.82° .

3.3.2 Implications of the dense Faraday screen

The widespread low fractional polarization seen in Fig. 8 shows an unusually large depolarization of the extended emission. The source of this depolarization is likely the dense Faraday screen in front of this emission. The chaotic nature of the thick Faraday screen seen in Figs 8 and 9 suggest a strong interaction between the radio sources and the cluster medium with small-scale variations in the foreground Faraday rotating medium. Since the Faraday rotation is proportional to the product of the magnetic field and the thermal electron density, this fine-scale structure could be from variations in the magnetic field, electron density, or both. The sightline to a polarized knot in the inner jet of the northern source (Fig. 9b) shows a relatively simple Faraday spectrum. This might be due to a foreground Faraday screen with a characteristic scale, smaller than the beamwidth but larger than the jet dimensions. If this is the case, the emission from a bright, unresolved jet knot then all sees the same Faraday depth, so the peak in the Faraday spectrum appears unresolved. Reversals in the sign of the Faraday depth indicate reversals in the magnetic field direction.

The complex Faraday screens are similar to that seen in other Abell clusters such as Abell 3667 (De Gasperin et al. 2022). This suggests that the radio emission from the PKS 2130–538 pair of galaxies is largely shaped by the interaction of the jets with the intracluster medium (ICM) in the host cluster, Abell 3785. However, additional

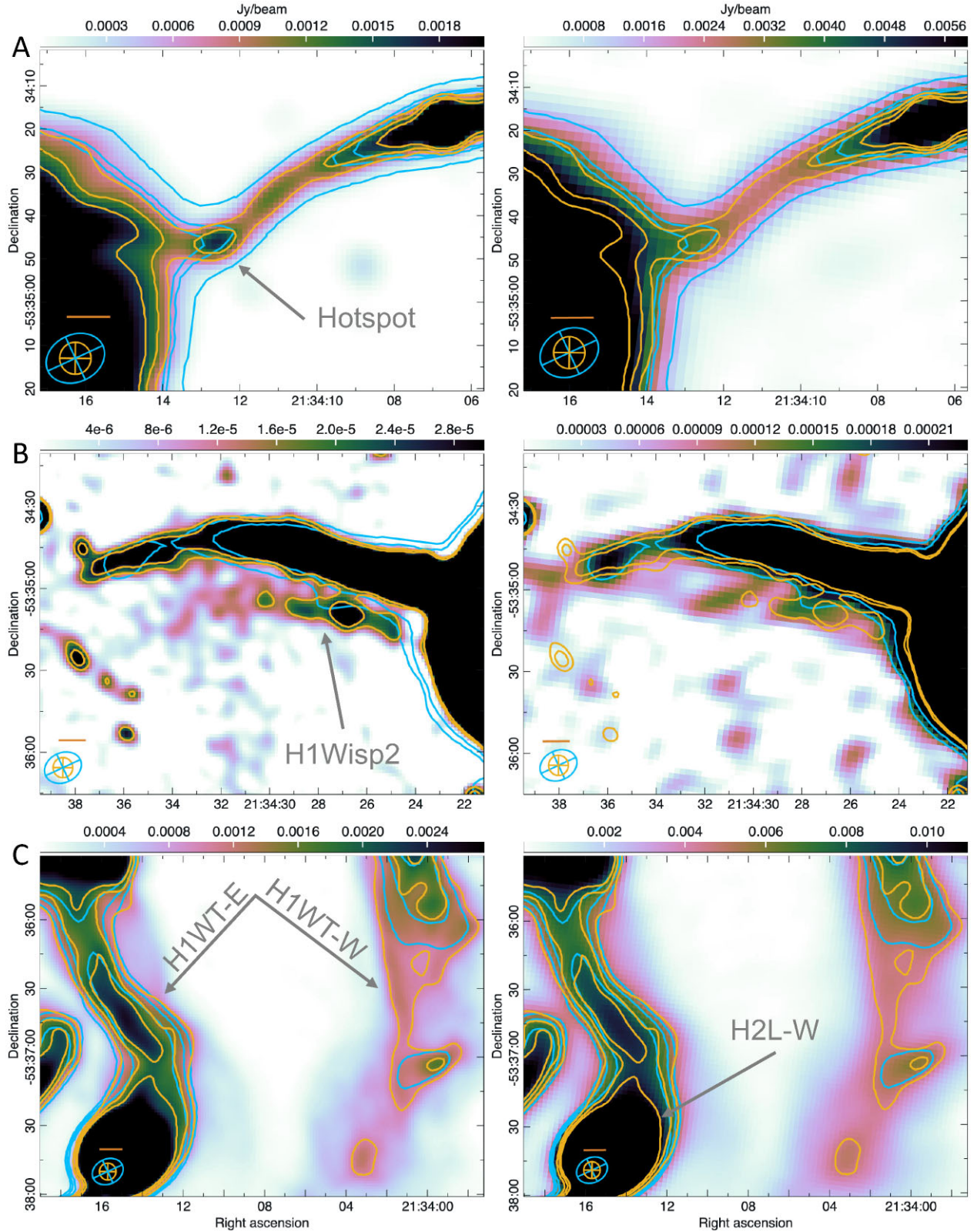


Figure 6. Dancing Ghosts subset images corresponding to regions marked as A, B, and C on Fig. 4. Subset images from MeerKAT (left-hand column) and ASKAP (right-hand column) are overlaid with orange (MeerKAT) and cyan (ASKAP) contours. In the bottom left corner, we show synthesized beam sizes of 13.95×10.90 arcsec² at PA = -58.15° as blue ellipses from ASKAP, and 7.5×7.1 arcsec² at PA = 0.82° as orange ellipses from MeerKAT data. The line above the synthesized beam sizes has an angular size of 10 arcsec. Contour levels for each panel are as follows: top panel: orange (0.000016, 0.000025) Jy beam⁻¹, cyan (0.00015, 0.000275) Jy beam⁻¹, middle panel: orange (0.0008, 0.0012, 0.0016) Jy beam⁻¹, cyan (0.0015, 0.003, 0.0035) Jy beam⁻¹, bottom panel: orange (0.001, 0.0015, 0.002) Jy beam⁻¹, cyan (0.005, 0.006, 0.00756.5) Jy beam⁻¹.

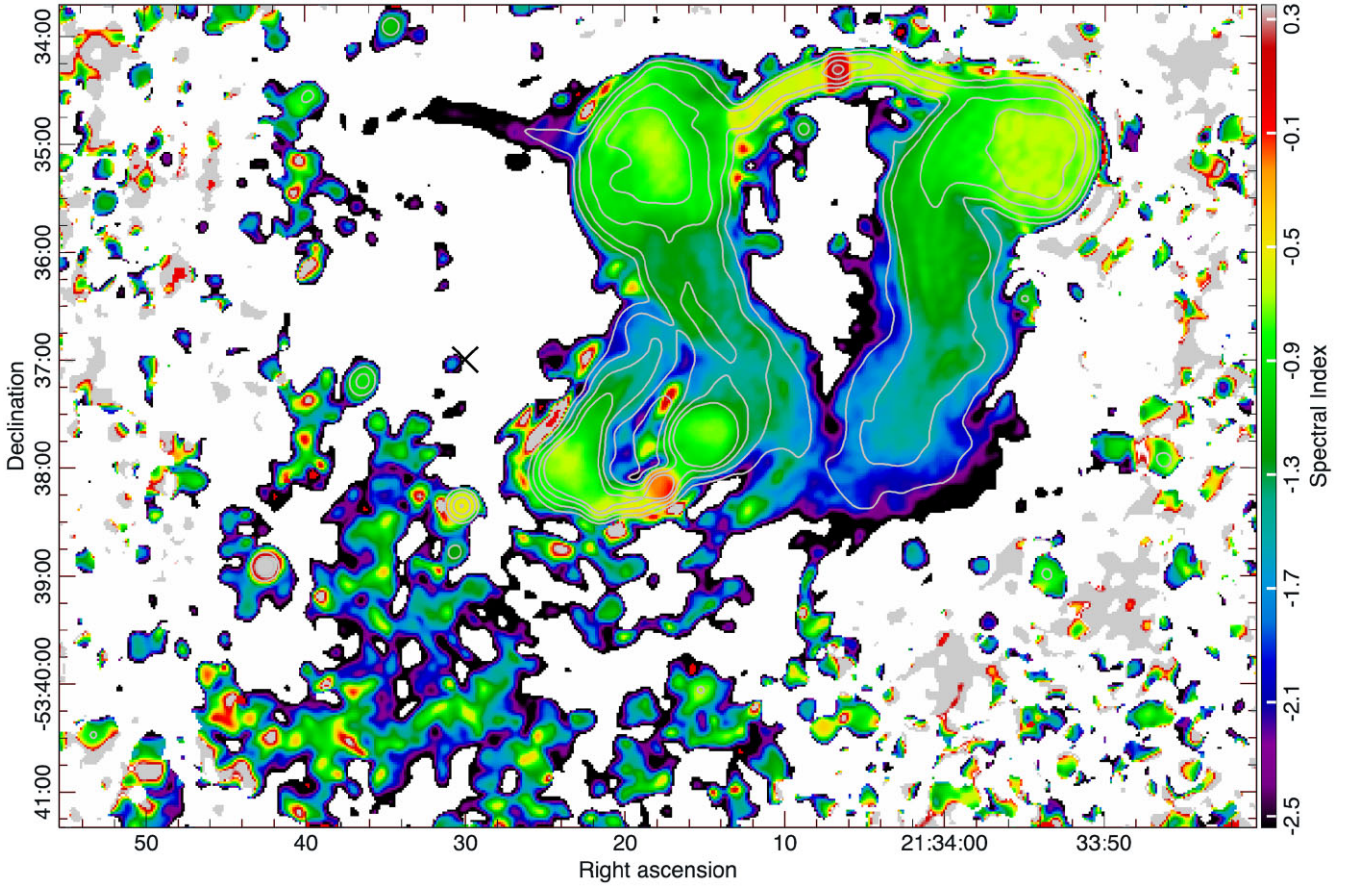


Figure 7. Spectral index map created using MeerKAT’s 800 MHz bandwidth images with Briggs’s robust weighting of 0 centred at $\nu = 1284$ overlaid with grey contours from total intensity image (0.00015, 0.00055, 0.0015, 0.002, 0.0045 Jy beam $^{-1}$). The synthesized beam size is (8.8×7.6 arcsec 2) at PA = -33.5° .

Table 2. Flux densities (peak and integrated) of different regions of PKS 2130–538, with an estimated uncertainty of 10 per cent. In Column 2, we show the region notation marked in Fig. 4. The spectral index is calculated independently from Fig. 7.

Region	Region Notation as in Fig. 4	$S_{p\text{MeerKAT}}$ (Jy beam $^{-1}$)	$S_{I\text{MeerKAT}}$ (Jy)	$\alpha \pm \Delta\alpha$
Host 1: core	H1C	0.0072	0.0077	+0.2 \pm 0.1
Host 1: jets	H1J	0.0072	0.0294	-0.7 \pm 0.1
Host 1: eastern lobe	H1L-E	0.0141	0.4060	-1.0 \pm 0.2
Host 1: western lobe	H1L-W	0.0103	0.3498	-0.9 \pm 0.2
Host 1: eastern wide tail	H1WT-E	0.0027	0.0986	-1.7 \pm 0.3
Host 1: western wide tail	H1WT-W	0.0024	0.0027	-1.8 \pm 0.4
Host 1: wisp 1	H1Wisp1	0.0004	0.0027	-2.5 \pm 0.5
Host 1: wisp 3	H1Wisp3	0.0002	0.0005	-2.3 \pm 0.2
Host 2: core	H2C	0.0023	0.0292	-0.2 \pm 0.1
Host 2: jets	H2J	0.0062	0.0167	-0.7 \pm 0.2
Host 2: eastern lobe	H2L-E	0.0381	0.2928	-0.8 \pm 0.1
Host 2: western lobe	H2L-W	0.0312	0.2312	-0.9 \pm 0.1
Host 2: eastern wide tail	H2WTE	0.0149	0.0779	-1.6 \pm 0.3

X-ray observations and analysis of Abell 3785 are needed to confirm the jet–ICM interaction.

We also obtained the expected Galactic foreground RM obtained using the CIRADA cutout server.² At the position of the Dancing Ghosts, the Galactic foreground RM is 15 ± 6 rad m $^{-2}$.

²<http://cutouts.cirada.ca/rmcutout/>

4 DISCUSSION

4.1 Signs of interaction in the Dancing Ghosts?

The projected distance between Host 1 and Host 2 is about $d \approx 369$ kpc (4.2 arcmin) in the plane of the sky. Because the only available redshifts are photometric with a typical uncertainty of $\delta z \approx 0.01 = 3000$ km s $^{-1}$, the peculiar velocity difference of

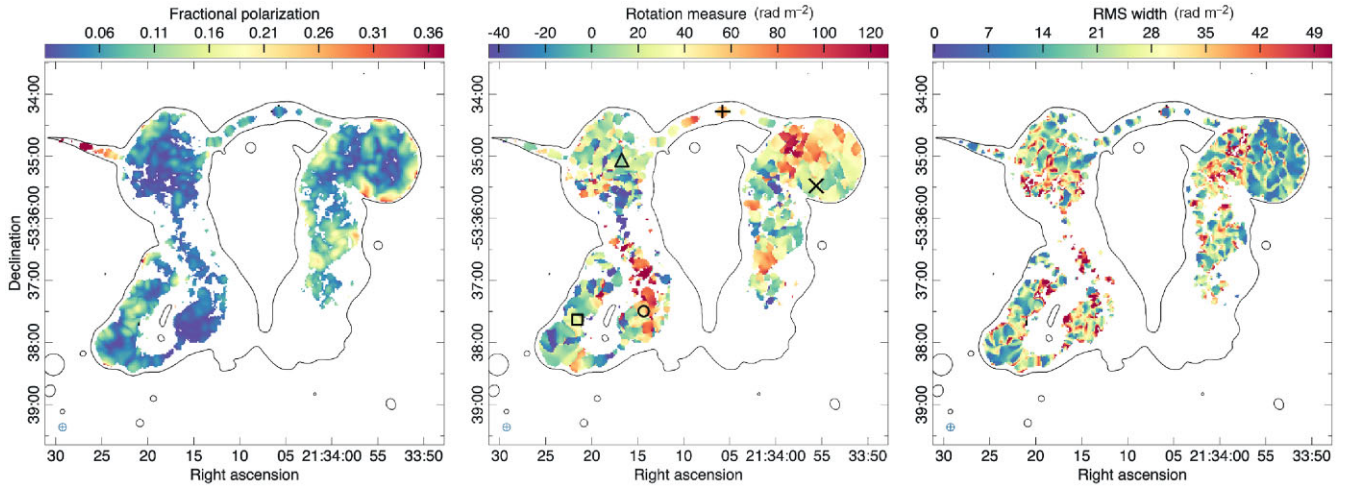


Figure 8. Left: Fractional polarization map of the Dancing Ghosts at the nominal frequency of 1283 MHz. Middle: Peak rotation measure map of the Dancing Ghosts created using MeerKAT polarization cubes. Black symbols indicate where plots of the Faraday spectra are given in Fig. 9. Positive values of RM represent a magnetic field oriented towards the observer. Right: The rms width of the feature in the Faraday spectrum in rad m^{-2} colour-coded by the colour bar at the top. The rms width of the restoring function used in the CLEAN deconvolution is 6 rad m^{-2} . All three images were overlaid with black contour from the total intensity image at 20σ , with $\sigma = 5.5 \mu\text{Jy beam}^{-1}$ to outline the source. The synthesized beam size is shown in the bottom left corner as a blue ellipse ($7.5 \times 7.5 \text{ arcsec}^2$) at $\text{PA} = -5.71^\circ$.

$\approx 580 \text{ km s}^{-1}$ inferred from redshifts is not significant. We therefore have no information on the radial separation of the two hosts.

To better understand the spatial structure of the Dancing Ghosts and their possible interactions, we further analysed spectral index (Fig. 7) and fractional polarization maps (Fig. 8) and used the Sobel matrix filter on total intensity image (Fig. 10). We looked for signs of discontinuities, in the form of sharp changes in polarization or spectral index, and filamentary structure within the region of interest (H2L-W and H1WT-E).

We note a slight increase in the polarization intensity and change of magnetic field orientation in the H1WT-E region (Figs 8), but no obvious discontinuities that would indicate possible interaction of the jets. Spectral index profiles along the H1WT-E region are relatively constant at about $\alpha \approx -1.7 \pm 0.1$, and in the transverse cuts, they go from $\alpha \approx -1.7$ at the ridge line to $\alpha \approx -2.3$ at the edges.

Additionally, in Fig. 10 we note a number of filamentary structures, inside the Dancing Ghosts galaxy pair. Filaments in the above-mentioned region, H1WT-E, do not show signs of intertwining. We also note that Host 1 lobes and wide tails would look symmetric if we subtract the emission from Host 2.

After analysing the region where the interaction is most likely to occur, we do not have strong evidence for the interaction between the galaxy pair. The absence of discontinuities in polarization, spectral index, and total intensity images, as well as inconclusive results from differences in peculiar velocities, suggests that the two galaxies are physically separate. We probably see the PKS 2130–538 complex as a projection effect along the line of sight. Nevertheless, further light may be shed on the level of interaction between the pair by magnetohydrodynamic simulations and modelling.

4.2 The nature of diffuse emission near the Dancing Ghosts

In this subsection, we discuss the diffuse emission marked with a blue polygon in Fig. 3. It is $\approx 7 \text{ arcmin}$ across ($D_A \approx 615 \text{ kpc}$ at the distance of Abell 3785) and shows an emission that is stronger than the calibration artefacts and over three times above the local rms ($\sigma \approx 5.5 \mu\text{Jy}$).

We also used the multiresolution filtering method of Rudnick (2002) to enhance the diffuse emission around the Dancing Ghosts. Fig. 11 shows the resulting image revealing the low surface brightness emission region south-east of PKS 2130–538 with a distinctive structure.

The origin of the extended and low surface brightness emission is unclear. Here, we present a few possible origins of this diffuse emission.

Since the diffuse emission is unpolarized and near the centre of the Abell 3785 cluster and its BCG (Host 2), it is possible that the emission represents the cluster’s radio halo. The slight offset between the centre (marked X in Fig. 3) of the cluster and its radio halo emission indicates that it could have suffered a recent merger event, and has not had enough time to relax (Poole et al. 2006; Molnar 2016). Future studies of the cluster using X-ray data could indicate if the emission is indeed coming from the halo.

Another possibility is that the emission is a remnant radio galaxy that is being compressed and distorted by either a merger shock or interaction with either Host 2 or ICM winds. If this were the case, the strength of the magnetic field and the momentum of the relativistic electrons in this plasma would increase, resulting in synchrotron emission (Rahaman et al. 2022). To calculate the spectral index of the diffuse emission we used the images with Brigg’s ‘optimal’ Robust weighting of 0 (AIPS/OBIT) which gives better overall sensitivity, as well as better surface brightness sensitivity at a cost of reduced resolution. In Fig. 12, we show that the integrated spectral index in the diffuse region is very steep $\alpha \approx -2.4$, favouring the relic origin of the emission.

For a galaxy to be classified as a remnant or fossil galaxy it needs to have its lobes detached from the AGN core, with no activity in the nucleus or jets (Murgia et al. 2011; Riseley et al. 2022). We also note that the region of diffuse emission might be connected to an ancient lobe originating from either of the two PKS 2130–538 hosts.

Finally, we suggest that this extended emission might originate from a neighbouring galaxy in the Abell 3785 cluster. Just $\approx 15 \text{ arcmin}$ to the south-east, there is another Abell 3785 member WISEA J213541.80–534413.2 at $z = 0.06254$ ($D_c \approx 264 \text{ Mpc}$) that shows an AGN jet pointing towards this extended emission

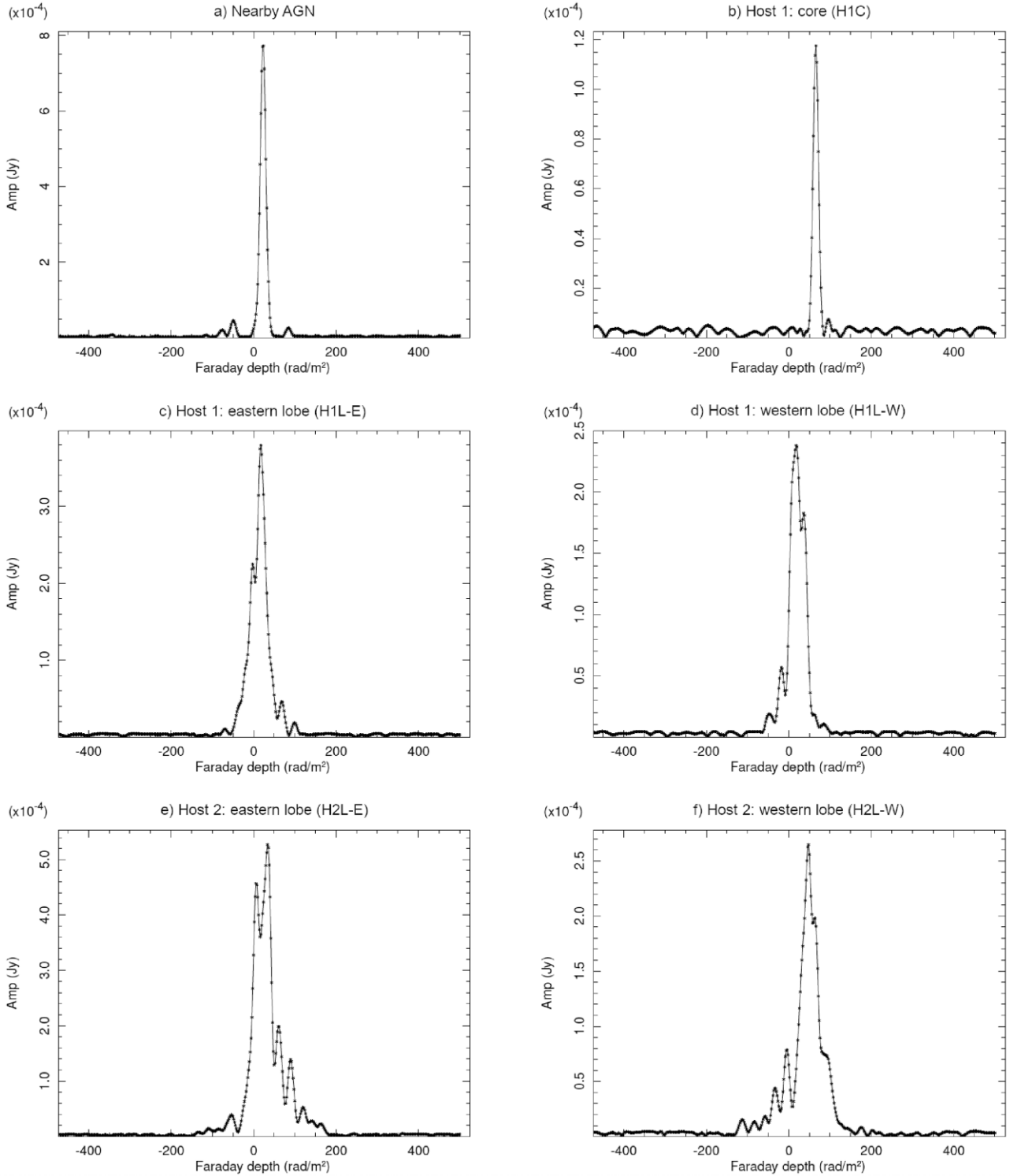


Figure 9. Faraday amplitude spectra with the exact location of sightlines indicated with black symbols in the middle panel of Fig. 8. (a) Nearby AGN, RA = $21^{\text{h}}35^{\text{m}}47^{\text{s}}.98$, Dec. = $-53^{\circ}28'44''.0$, (b) polarized knot in inner jet, near the core of northern source (H1C), ‘+’ in Fig. 8, (c) eastern lobe of northern source (H1L-E), triangle in Fig. 8, (d) western lobe of northern source (H1L-W), ‘X’ in Fig. 8, (e) eastern lobe of southern source (H2L-E), square in Fig. 8, (f) western lobe of southern source (H2L-W), circle in Fig. 8. Sightlines through the lobes of the Dancing Ghosts (panels: 9c–9f) show components with thick Faraday structures spreading over 100 rad m^{-2} .

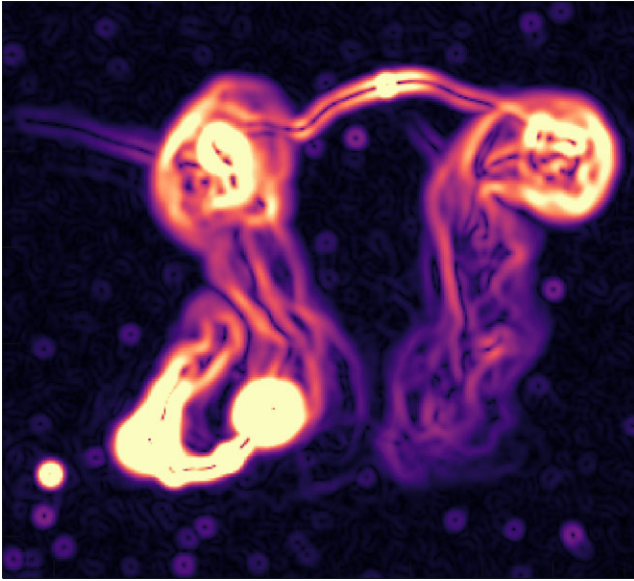


Figure 10. Image generated by a Sobel edge-detection filter of the Dancing Ghosts, to emphasize the filamentary structures in radio galaxy complex. This was generated using the NINER task in AIPS with synthesized beam size $7.5 \times 7.1 \text{ arcsec}^2$.

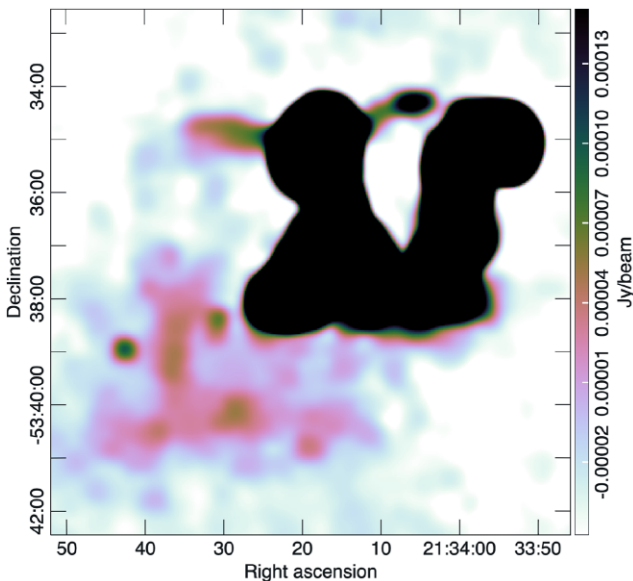


Figure 11. Resulting image of the Dancing Ghosts after using the multiresolution filtering method to subtract point sources and enhance diffuse emission from the total intensity image. The synthesized beam size is convolved to $18 \times 18 \text{ arcsec}^2$.

and directly via other Abell 3785 member J213522.85–534200.3 at the redshift $z = 0.08114$ ($D_c \approx 341 \text{ Mpc}$) (see Fig. 3 top left inset). The prominent jet of WISEA J213541.80–534413.2 shows a flat spectral index at its core ($\alpha = 0.15$) and steepens with distance as the jet propagates to $\alpha = -2$. While possible, it is unlikely that the diffuse emission originates from WISEA J213541.80–534413.2.

The fact that Host 2 is the BCG of the Abell 3785 cluster implies that the emission is most likely affected by shocks, which raises the possibility the origin of the diffuse emission is either from a radio halo or a fossil galaxy. It is important to note that we could not find a cluster’s radio halo with a similar shape in the literature.

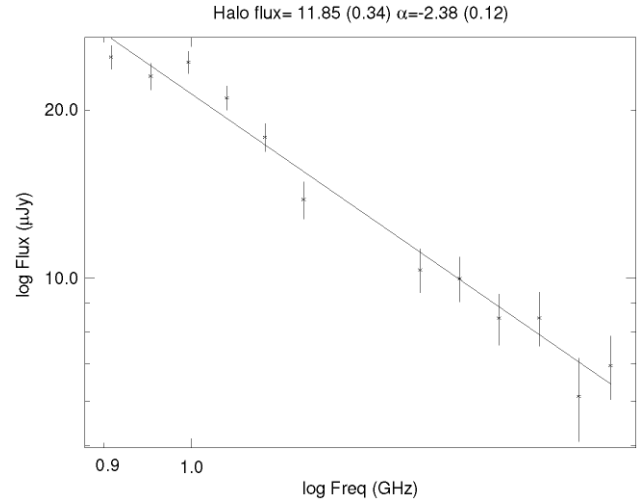


Figure 12. Spectrum of the diffuse emission southeast of the Dancing Ghosts, blue polygon region in Fig. 3, calculated between 886 and 1681 MHz in 14 sequential channels described in Table 1.

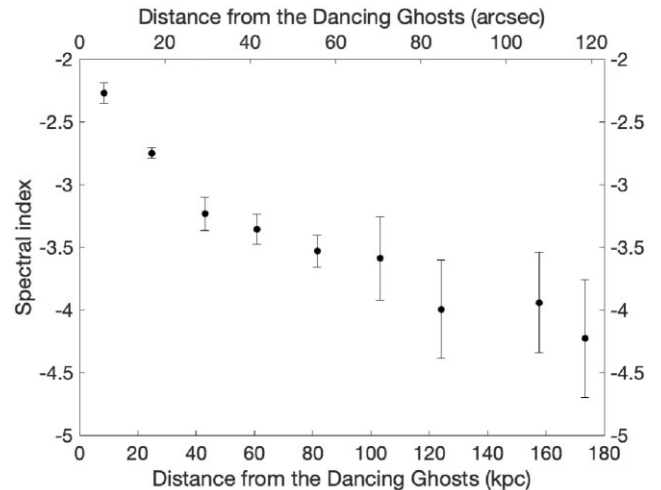


Figure 13. Spectral index of the wisp (H1Wisp1) as the function of the distance from the lobe of the Dancing Ghosts. Calculated between 886 and 1681 MHz in 14 sequential channels described in Table 1.

4.3 The nature of wisps

Here, we discuss the thin, faint features originating from the lobes (marked in Fig. 4 as H1Wisp1–H1Wisp4). These thin synchrotron filaments are emerging new phenomena in radio images with sufficient resolution and sensitivity. They have been detected in recent studies of various galaxy clusters and AGN (e.g. Abell 3376, IC 4296, ESO 137–006 by Ramatsoku et al. 2020; Condon et al. 2021; De Gasperin et al. 2022, respectively). Furthermore, Rudnick et al. (2022) thoroughly examine the thin synchrotron filaments and discuss the most likely scenarios of their origins. Yusef-Zadeh, Arendt & Wardle (2022) compare well-studied Galactic and recently discovered extragalactic synchrotron filaments. They argue that both phenomena originate from the same physical processes but on drastically different scales.

The Meerkat Observations of the Dancing Ghosts and filamentary structure suggest that H1Wisp1 has a broad envelope extending across H1Wisp2. Fig. 13 shows the spectral index of the H1Wisp1

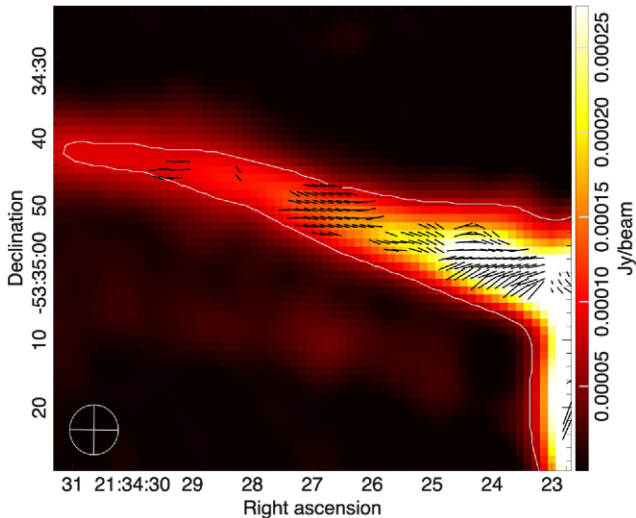


Figure 14. Total intensity image of the wispl (H1Wispl) overlaid with magnetic field vectors after RM correction and the grey contours at $78 \mu\text{Jy}$. The synthesized beam size is shown in the bottom left corner as a white ellipse ($7.5 \times 7.1 \text{ arcsec}^2$ at $\text{PA} = 0.82^\circ$).

as a function of the distance from the lobe of the Dancing Ghost.

Fig. 14 shows the magnetic field vectors derived from polarization data and de-rotated for the Faraday rotation effect. Magnetic field vectors are relatively ordered and oriented along the filamentary structure. It should be noted that due to the unresolved Faraday spectra in the region of filaments and our derivation is unambiguous. These characteristics are very similar to what Rudnick et al. (2022) detected in filaments of 3C40B.

The steepening of spectral index could come from two causes, which cannot be easily disentangled: (1) a curved electron spectrum seen in progressively weaker magnetic fields, thus showing steeper spectral indices as the fields get weaker and the radiation samples the higher energy part of the spectrum, and (2) radiative ageing if there is a flow of material from the radio galaxy.

Systematic changes in brightness and spectrum as a function of distance from the bright radio galaxy structure suggest that the wispl (H1Wispl) is part of the Dancing Ghosts and not a superposition with a background source.

Magnetized filaments composed of smaller fibres are created in turbulent, highly pressurized and magnetic plasmas, and could also be further stretched by the jet encounter with the dense cloud moving within ICM. However, this scenario does not explain the spectral structure and the flux density change as a function of the distance from the lobe of the Dancing Ghosts.

Other explanations include the interaction between the jets and the dense ICM cloud, either stationary or moving and cosmic ray acceleration of the diffuse emission originating from the PKS 2130–538.

In the scenario where the jet hits a very dense cloud, we expect deflection – bending of the jets. The Dancing Ghost pair abruptly changes the flow direction near the most prominent wisps, H1Wispl and H1Wispl3. We note that H1Wispl3 is possibly reconnecting with the core of Host 1, which might be the source of cosmic rays for reacceleration of electrons within a low-diffuse emission, but for the remaining wisps there has to be interaction with the ICM.

The strong evidence for the existence of intracluster galactic wind and the turbulent ICM is that all the wisps originating in the Dancing

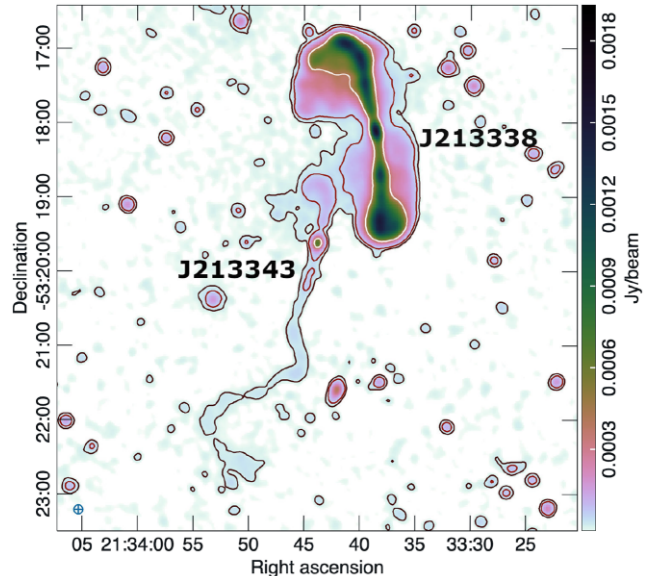


Figure 15. Image of the two extended radio sources within Abell 3785 and NW of the Dancing Ghosts. Contour levels are at $[3, 10, 85] \times \sigma$, with $\sigma = 4.78 \mu\text{Jy beam}^{-1}$, presented from dark to light colour. The synthesized beam size is shown in the bottom left corner as a blue ellipse ($7.5 \times 7.1 \text{ arcsec}^2$) at $\text{PA} 0.82^\circ$.

Ghosts point from the lobes towards the north-east regardless of the jet flow in the local area.

4.4 North-west sources of Abell 3785

The two brightest radio sources show clear two-sided AGN jets, which are pointing towards PKS 2130–538 (Fig. 15). These two are WISEA J213338.54–531806.2 (J213338; at $z = 0.0751$ or $D_c \approx 316 \text{ Mpc}$) and WISEA J213343.77–531937.1 (J213343; at $z = 0.0826$ or $D_c \approx 347 \text{ Mpc}$).

The two above-mentioned extended objects have steep radio spectra. J213338 has a spectral index at the core $\alpha = -1$ and relatively constant along the jets $\alpha = -1.2$ but steepening to $\alpha \leq -2$ at the edges of the jets, while J213343 on the other hand is relatively steep at the core $\alpha = -0.76$ and afterwards intermittently flattens and steepens in a twisted and collimated jet.

5 CONCLUSION

We use high-resolution and high-sensitivity MeerKAT observations to study the galaxy cluster Abell 3785 and its peculiar galaxy pair – PKS 2130–538, the Dancing Ghosts, previously detected in the ASKAP EMU pilot survey.

(i) MeerKAT observations reveal more detailed low surface brightness structures, filamentary structures, and a hotspot near the northern left lobe.

(ii) Of particular interest are a number of wisps emanating from the lobes of the radio galaxies. We do not currently have a satisfactory explanation of these.

(iii) Fractional polarization and Faraday analysis show a very complex magnetic field with a thick and dense Faraday screen resulting in a large depolarization of the extended emission within the Dancing Ghosts, which is also affected by ICM.

(iv) We see no sign of interaction between the two radio galaxies in the Dancing Ghosts, and, although both are associated with the

cluster, we suggest they may merely be superimposed along the line of sight.

(v) Diffuse emission near the Dancing Ghosts may represent a radio halo of the Abell 3785 cluster or a fossil radio galaxy.

(vi) We detect 30 radio continuum sources within Abell 3785 including the Dancing Ghosts.

ACKNOWLEDGEMENTS

We thank Lawrence Rudnick for providing useful discussions and insights which greatly contributed to this paper.

The MeerKAT telescope is operated by the South African Radio Astronomy Observatory, which is a facility of the National Research Foundation, an agency of the South Africa Department of Science and Innovation.

The National Radio Astronomy Observatory is a facility of the US National Science Foundation, operated under a cooperative agreement by Associated Universities, Inc.

The Australian SKA Pathfinder is part of the Australia Telescope National Facility which is managed by the Commonwealth Scientific and Industrial Research Organisation (CSIRO). The operation of ASKAP is funded by the Australian Government with support from the National Collaborative Research Infrastructure Strategy (NCRIS). ASKAP uses the resources of the Pawsey Supercomputing Centre. The establishment of ASKAP, the Murchison Radio-astronomy Observatory and the Pawsey Supercomputing Centre are initiatives of the Australian Government, with support from the Government of Western Australia and the Science and Industry Endowment Fund. We acknowledge the Wajarri Yamatji people as the traditional owners of the Observatory site.

This research has made use of the NASA/IPAC Extragalactic Database (NED), which is funded by the National Aeronautics and Space Administration and operated by the California Institute of Technology.

The DESI Legacy Imaging Surveys consist of three individual and complementary projects: the Dark Energy Camera Legacy Survey (DECaLS), the Beijing-Arizona Sky Survey (BASS), and the Mayall z -band Legacy Survey (MzLS). DECaLS, BASS and MzLS together include data obtained, respectively, at the Blanco telescope, Cerro Tololo Inter-American Observatory, NSF's NOIRLab; the Bok telescope, Steward Observatory, University of Arizona; and the Mayall telescope, Kitt Peak National Observatory, NOIRLab. NOIRLab is operated by the Association of Universities for Research in Astronomy (AURA) under a cooperative agreement with the National Science Foundation. Pipeline processing and analyses of the data were supported by NOIRLab and the Lawrence Berkeley National Laboratory (LBNL). Legacy Surveys also uses data products from the Near-Earth Object Wide-field Infrared Survey Explorer (NEOWISE), a project of the Jet Propulsion Laboratory/California Institute of Technology, funded by the National Aeronautics and Space Administration. Legacy Surveys was supported by: the Director, Office of Science, Office of High Energy Physics of the U.S. Department of Energy; the National Energy Research Scientific Computing Center, a DOE Office of Science User Facility; the U.S. National Science Foundation, Division of Astronomical Sciences; the National Astronomical Observatories of China, the Chinese Academy of Sciences and the Chinese National Natural Science Foundation. LBNL is managed by the Regents of the University of California under contract to the U.S. Department of Energy. The complete acknowledgments can be found at <https://www.legacysurvey.org/acknowledgment/>.

© The Author(s) 2023.

Published by Oxford University Press on behalf of Royal Astronomical Society. This is an Open Access article distributed under the terms of the Creative Commons Attribution License (<http://creativecommons.org/licenses/by/4.0/>), which permits unrestricted reuse, distribution, and reproduction in any medium, provided the original work is properly cited.

We thank the anonymous referee for the insightful comments and suggestions that significantly improved our paper and its presentation.

DATA AVAILABILITY

The software utilized in the paper are available at <https://www.cv.nrao.edu/~bcotton/Obit.html>. The radio imaging products presented here are made publicly available with this paper at <https://doi.org/10.48479/akx9-hd96>, including spectral index and Stokes I, Q, and U L -band cubes.

REFERENCES

- Abell G. O., Corwin Harold G. J., Olowin R. P., 1989, *ApJS*, 70, 1
 Bautz L. P., Morgan W. W., 1970, *ApJ*, 162, L149
 Bilicki M., Jarrett T. H., Peacock J. A., Cluver M. E., Steward L., 2014, *ApJS*, 210, 9
 Brentjens M. A., de Bruyn A. G., 2005, *A&A*, 441, 1217
 Comrie A. et al., 2021, *CARTA: The Cube Analysis and Rendering Tool for Astronomy*, Zenodo
 Condon J. J., Cotton W. D., White S. V., Legodi S., Goedhart S., McAlpine K., Ratcliffe S. M., Camilo F., 2021, *ApJ*, 917, 18
 Cotton W. D. et al., 2018, *ApJ*, 856, 67
 De Gasperin F. et al., 2022, *A&A*, 659, A146
 Dey A. et al., 2019, *AJ*, 157, 168
 Donnelly R. H., Partridge R. B., Windhorst R. A., 1987, *ApJ*, 321, 94
 Ekers R. D., 1970, *Aust. J. Phys.*, 23, 217
 Filipović M. D. et al., 2022, *MNRAS*, 512, 265
 Hardcastle M. J., Croston J. H., 2020, *New Astron. Rev.*, 88, 101539
 Heywood I. et al., 2022, *ApJ*, 925, 165
 Ishwara-Chandra C. H., Saikhi D. J., Kapahi V. K., McCarthy P. J., 1998, *MNRAS*, 300, 269
 Jonas J., MeerKAT Team, 2016, MeerKAT Science: On the Pathway to the SKA. p. 1
 Jones D. H. et al., 2009, *MNRAS*, 399, 683
 Jones P. A., McAdam W. B., 1992, *ApJS*, 80, 137
 Lauer T. R., Postman M., Strauss M. A., Graves G. J., Chisari N. E., 2014, *ApJ*, 797, 82
 Mauch T. et al., 2020, *ApJ*, 888, 61
 Molnar S., 2016, *Front. Astron. Space Sci.*, 2, 7
 Murgia M. et al., 2011, *A&A*, 526, A148
 Norris R. P. et al., 2021, *Publ. Astron. Soc. Aust.*, 38, e046
 Norris R. P. et al., 2022, *MNRAS*, 513, 1300
 Poole G. B., Fardal M. A., Babul A., McCarthy I. G., Quinn T., Wadsley J., 2006, *MNRAS*, 373, 881
 Prandoni I., Parma P., Wieringa M. H., de Ruiter H. R., Gregorini L., Mignano A., Vettolani G., Ekers R. D., 2006, *A&A*, 457, 517
 Rahaman M., Raja R., Datta A., Burns J. O., Rapetti D., 2022, *MNRAS*, 515, 2245
 Ramatsoku M. et al., 2020, *A&A*, 636, L1
 Riseley C. J. et al., 2022, *MNRAS*, 515, 1871
 Rudnick L. et al., 2022, *ApJ*, 935, 168
 Rudnick L., 2002, *PASP*, 114, 427
 Rudnick L., Cotton W. D., 2023, *MNRAS*, 522, 1464
 Schilizzi R. T., McAdam W. B., 1975, *MNRAS*, 79, 1
 Taylor G. B., Perley R. A., Inoue M., Kato T., Tabara H., Aizu K., 1990, *ApJ*, 360, 41
 White S. V. et al., 2020a, *Publ. Astron. Soc. Aust.*, 37, e017
 White S. V. et al., 2020b, *Publ. Astron. Soc. Aust.*, 37, e018
 Yusef-Zadeh F., Arendt R. G., Wardle M., 2022, *ApJ*, 939, L21

This paper has been typeset from a $\text{\TeX}/\text{\LaTeX}$ file prepared by the author.